

1 **Title Page**

2 **Title**

3 Targeted Nanofitin-drug conjugates achieve efficient tumor delivery and therapeutic effect in an EGFR^{pos}
4 mouse xenograft model

5 **Authors and affiliations**

6 Simon Huet^{1*}, Magali Zeisser Labouebe^{2,3}, Rute Castro⁴, Perrine Jacquot¹, Jessy Pedrault¹, Sébastien
7 Viollet¹, Gaetan Van Simaey⁵, Gilles Doumont⁵, Lionel Larbanoix⁶, Egor Zindy⁵, António E. Cunha⁴,
8 Leonardo Scapozza^{2,3}, Mathieu Cinier¹.

9 ¹Affilogic SAS; Nantes, France.

10 ²Pharmaceutical Biochemistry Group, School of Pharmaceutical Sciences, University of Geneva; Geneva,
11 Switzerland.

12 ³Institute of Pharmaceutical Sciences of Western Switzerland, University of Geneva; Geneva, Switzerland.

13 ⁴iBET, Instituto de Biologia Experimental e Tecnológica; Oeiras, Portugal.

14 ⁵CMMI, Center for Microscopy and Molecular Imaging, Université libre de Bruxelles; Charleroi
15 (Gosselies), Belgium.

16 ⁶CMMI, Center for Microscopy and Molecular Imaging, Université de Mons; Charleroi (Gosselies),
17 Belgium.

18 *Corresponding author.

19 **Running title**

20 Nanofitin-drug conjugates achieve targeted anti-tumor effect

21 **Abbreviations list**

ADC	Antibody-Drug Conjugate
ADCC	Antibody-Dependent Cell Cytotoxicity
ANOVA	ANalysis Of VAriance
BLI	BioLuminescence Imaging
BSA	Bovine Serum Albumin
CAR-T	Chimeric Antigen Receptor expressing T cells
CD31/PECAM	Platelet Endothelial Cell Adhesion Molecule-1
DMSO	DiMethyl SulfOxide
<i>E. coli</i>	<i>Escherichia coli</i>
EGFR	Epithelial Growth Factor Receptor
EPR	Enhanced Permeability and Retention
ESI+	ElectroSpray Ionization in positive ion mode
FFPE	Formalin-Fixed and Paraffin-Embedded
HEPES	4-(2-HydroxyEthyl)-1-PiperazineEthaneSulfonic acid
IHC	ImmunoHistoChemistry
IPTG	IsoPropyl β -d-1-ThioGalactopyranoside
irrNF	Irrelevant Nanofitin
K_D	Dissociation equilibrium constant
k_{off}	Off-rate constant
k_{on}	On-rate constant
LC	Liquid Chromatography
Luc+	Luciferase-positive
MMAE	MonoMethyl Auristatin E
MMAF	MonoMethyl Auristatin F
MS	Mass Spectrometry
MWCO	Molecular Weight Cut-Off
RP	Reverse Phase
SDS-PAGE	Sodium Dodecyl Sulfate-PolyAcrylamide Gel Electrophoresis
TBS	Tris-Buffered Saline
TCEP	Tris(2-CarboxyEthyl)Phosphine
TFF	Tangential Flow ultraFiltration
TIC	Total Ion Current
UPLC	Ultra-high Performance Liquid Chromatography
vc-MMAE	MonoMethyl Auristatin E and valine-citrulline linker, or mc-vc-PAB-MonoMethyl Auristatin E

22 **Corresponding author**

23 Simon HUET ; AFFILOGIC, 24 rue de la Rainière, 44300 Nantes, FRANCE ; Phone: +33 7 82 94 53 05 ;

24 Email: simon@affilogic.com

25 **Conflict of interest statement**

26 SH, PJ, JP, SV, and MC hold employment in Affilogic. The Nanofitin technology described in this study,
27 commercialized by Affilogic, uses the patent application owned by Institut Pasteur and Centre National de
28 la Recherche Scientifique (CNRS): “OB-fold used as scaffold for engineering new specific binders”;
29 PCT/IB2007/004388. Affilogic SAS, Nantes, France, provided support for the study and participated in
30 study design, conducted the study, and provided data collection, management and interpretation. This does
31 not alter the authors’ adherence to all the journal policies on sharing data and materials.

32 **Abstract**

33 Adjusting the molecular size, the valency and the pharmacokinetics of drug conjugates are as many
34 leverages to improve their therapeutic window, notably by affecting tumor penetration, renal clearance and
35 short systemic exposure. In that regard, small tumor-targeting ligands are gaining attention. In this study,
36 we demonstrate the benefits of the small Nanofitin alternative scaffolds (7 kDa) as selective tumor-targeting
37 modules for the generation of drug conjugates, focusing on Nanofitins B10 and D8 directed against the
38 Epithelial Growth Factor Receptor (EGFR). Owing to their small size and monovalent format, the two
39 Nanofitins displayed a fast and deep tumor penetration in EGFR-positive A431 xenografts in BALB/c nude
40 mice after intravenous administration, yielding to a targeting of respectively $67.9\% \pm 14.1$ and $98.9\% \pm 0.7$ of
41 the tumor cells as demonstrated by immunohistochemistry. Conjugation with the monomethyl auristatin E
42 toxin provided homogeneous Nanofitin-drug conjugates, with an overall yield of $\geq 97\%$, for *in vivo*
43 assessment in a curative xenograft model using bioluminescent, EGFR-positive, A431 cells in BALB/c nude
44 mice. Internalization was found critical for efficient release of the toxin. Hence, the intravenous

45 administration of the D8-based construct showed significant anti-tumor effect *in vivo* as determined by
46 monitoring tumor volumes and bioluminescence levels over 2 months.

47 **Introduction**

48 The treatment of solid tumors with pharmacological modalities remains challenging, notably because their
49 antigenic heterogeneity (1) and limited permeability to macromolecules (2) can lead to a suboptimal drug
50 exposure. While chemotherapeutics benefit from the advantage of a broad diffusion within the tumor tissue,
51 their lack of specificity is limiting their therapeutic window (3, 4). Their mechanism of action is mostly
52 restricted to the killing of dividing cells, which hampers their effect on dormant and slow-dividing cancer
53 cells (5). Antibody-based immunotherapies have the potential to preferentially target the tumor cells but
54 display a slow diffusion in tumors (6), leaving some of the deepest tumor cells unexposed to the drug.
55 Limited diffusion of antibodies is attributed to distinct factors (7). First, their high molecular weight hinders
56 their passive diffusion from the blood vessel even if facilitated by the well-known Enhanced Permeability
57 and Retention (EPR) effect. Second, the diffusion of the antibody within the tumor tissue can be restricted
58 by the so-called barrier site effect (8), referring to the trapping of the antibody in the surrounding of the
59 vasculature. Moreover, the cytotoxic activity of antibody-based therapeutics often relies on antibody-
60 dependent cell cytotoxicity (ADCC), which can be crippled in the context of an immunosuppressive tumor
61 microenvironment (9). To restore cytotoxic activity, combining chemo- and immunotherapies is now the
62 standard of care for many cancer diseases.

63 Since the approval of Kadcyra[®] in 2013, antibody-drug conjugates (ADCs) have been used to combine the
64 well-established nature and selectivity of antibody therapeutics with the high cytotoxic potency of small
65 molecule toxins. Despite showing promise and undergoing continuous improvements as a disruptive
66 technology in oncology (10), the use of ADCs for treating solid tumors remains limited by inherent
67 constraints of antibodies. In addition to their poor extravasation (11), ADCs display antibody-like
68 pharmacokinetic profiles with a prolonged plasma half-life that can foster off-target release of the toxin and

69 subsequent toxicity (12, 13). Besides, antibodies undergo a systemic clearance mainly driven by hepatic
70 metabolism (14), leading to hepatic and gastrointestinal toxicities in the case of an ADC that can limit its
71 therapeutic window. Finally, the tripartite assembly of the ADC (antibody-linker-cytotoxic payload)
72 requires a demanding process that can result in ADCs of lower solubility and homogeneity than their parent
73 antibodies and the generation of immunogenic aggregates (15).

74 Next generation drug conjugate therapies would benefit from a better control of their homogeneity,
75 biodistribution and cell engagement (16). An alternative strategy consists in replacing the antibody with a
76 ligand of less than 10 kDa (17–20) allowing faster accumulation and broader diffusion within the tumor
77 together with a lesser systemic exposure compared to conventional antibodies (21, 22). As a support to this
78 rationale, robust preclinical efficiency has been demonstrated with the bicycle peptide-toxin conjugates
79 BT1718 and BT5528 (23) currently evaluated in clinical trials against solid tumors (24, 25).

80 In this publication, we describe the use of Nanofitins for the engineering of drug conjugates, as they benefit
81 from the desired properties of non-antibody alternative scaffolds (26): small, single chain, cysteine-free and
82 without post-translational modification. Nanofitins can be engineered to bind with high affinity and
83 specificity to a wide variety of biologically relevant targets (27–34). They are amenable to regioselective
84 enzymatic or chemical conjugation by the introduction of a unique acceptor sequence (sortase-tag,
85 cysteine...) using straightforward molecular approaches, while preserving the original pharmacologic and
86 stability properties of the parent protein. Their extreme resistance to temperature ($T_m > 70^\circ\text{C}$), pH (1-13)
87 and their ability to spontaneously fold in aqueous solutions make them naturally compatible with a broad
88 range of conjugation reaction conditions, as well as with synthetic manufacturing.

89 In a previous study, we demonstrated with a radiolabeled, non-internalizing, Nanofitin targeting the
90 Epithelial Growth Factor Receptor (EGFR) that high tumor-to-blood contrast can be achieved as fast as 90
91 min post-injection (32), thanks to its fast tumor uptake and rapid elimination from the bloodstream.
92 Clearance was mainly mediated by renal excretion, which is a promising feature to avoid hepatic toxicity.

93 Here, we describe the development of a Nanofitin-drug conjugate based on an internalizing anti-EGFR
94 Nanofitin. We illustrate the superior diffusion rate of anti-EGFR Nanofitins in commonly used A431-
95 derived solid tumors, in comparison to the therapeutic antibody Cetuximab. Finally, we demonstrate the
96 regioselective conjugation to the combination of Monomethyl auristatin E and valine-citrulline linker (vc-
97 MMAE) moieties, widely used for ADCs (10), and the ability of the resulting D8-vc-MMAE conjugate to
98 promote a significant anti-tumor activity *in vivo*.

99 **Materials and Methods**

100 **Production and purification of tag-free Nanofitins**

101 *E. coli* DH5 α clones expressing tag-free Nanofitins D8, B10 and irrNF (irrelevant Nanofitin), bearing a C-
102 terminal cysteine (**Fig. S1**), were cultivated in M9 minimal medium, in shake-flasks (37 °C, 180 rpm).
103 Nanofitin expression was induced with IPTG (1 mM) for 4 h (D8) or 16 h (B10 and irrNF). Cells were
104 harvested by centrifugation using a Beckman Avanti J-HC. Biomass was disrupted in APV 2000
105 homogenizer, and cell debris removed by centrifugation (30 min, 31000g, 4 °C). Supernatants were clarified
106 by filtration through a 0.2 μ m filter. Filtrates were treated by tangential flow ultrafiltration (TFF) with 30
107 and 5 kDa MWCO membranes (Sartorius): after purification (30 kDa MWCO), samples were concentrated
108 and diafiltrated (5 kDa MWCO). Each Nanofitin was purified by cation exchange chromatography using
109 Fractogel SO₃⁻ resin (Merck EMD). Nanofitins D8 and B10 were polished by size exclusion
110 chromatography using a Superdex 75 column (Cytiva). Purified Nanofitins were formulated in 20 mM
111 HEPES containing 150 mM of NaCl, pH 7.4, concentrated by TFF (5 kDa MWCO) and loaded onto a
112 Sartobind STIC nano column (Sartorius) for endotoxin removal. Protein purity was addressed using standard
113 SDS-PAGE analysis and mass spectrometry. Endotoxin levels were assessed using the Endosafe-PTS LAL
114 analysis (Charles River).

115 **Binding affinity determination by biolayer interferometry**

116 Binding kinetic parameters of the anti-EGFR Nanofitins B10 and D8 drug conjugates, B10-vc-MMAE and
117 D8-vc-MMAE, were measured by interferometry (Octet RED96, ForteBio, RRID:SCR_023267).
118 Recombinant Human EGFR Fc chimera protein (344-ER, R&D Systems) was diluted to 5 µg/mL and loaded
119 on protein A biosensors at 1 nm before equilibration for 60 s. Binding kinetics were then evaluated by
120 simultaneously exposing biosensors to various concentrations (500, 125, 31.25, 7.81 and 0 nM) of B10-vc-
121 MMAE or D8-vc-MMAE. Association and dissociation steps were measured for 3 min each. Unless
122 otherwise specified, all steps were performed in TBS containing 0.002% Tween 20 and 0.01% BSA.
123 Biosensors were regenerated using three cycles of alternating washes for 10 s in Glycine 10 mM pH 2.5 and
124 in TBS. All the steps were run at 30°C and 1000 rpm. The biosensor exposed to the 0 nM concentration was
125 used as a background reference. Sensorgrams were processed using a single reference subtraction and
126 analyzed using the Octet Data Analysis software (ForteBio). Fitting was performed with a 1:1 binding fit
127 model and illustrated with GraphPad Prism 6 (GraphPad Inc, RRID:SCR_002798).

128 Affinities were also determined for cysteine-free and HA-tagged (35) Nanofitins (500, 250, 125, 62.5, 31.25,
129 15.63, 7.81 and 0 nM), either on human EGFR as described above, or on murine EGFR by using
130 Recombinant Mouse EGFR Fc chimera protein (1280-ER, R&D Systems) for the loading step.

131 **Nanofitin-Drug Conjugation**

132 *Conjugation*

133 Nanofitins bearing a C-terminal cysteine were treated by 10 mg batches (2 mg/mL) overnight at 4°C with
134 TCEP (4x molar excess from stock solution at 1 M). Five molar equivalents of mc-vc-PAB-MonoMethyl
135 Auristatin E (vc-MMAE, Ontario Chemicals) were added to the reduced Nanofitins from the stock solution
136 of vc-MMAE at 10 mg/mL in DMSO and left under agitation under argon (2 h, 25°C). The excess of
137 unconjugated vc-MMAE was removed on a spin PD-10 column (Sephadex™ G-25, GE Healthcare) before
138 purification of the NF conjugates by size exclusion chromatography on a HiLoad 16/60 Superdex 75 PG

139 column (GE Healthcare) with HEPES buffer at 1.2 mL/min. Fractions containing the Nanofitin-vc-MMAE
140 conjugates were pooled and concentrated to about 5 mg/mL using Pierce protein concentrators 3K. The final
141 product was characterized by UPLC-RP/MS. The Nanofitin-vc-MMAE conjugates were sterile-filtered and
142 stored at -80°C for further use.

143 Mass spectrometry

144 Product identity (**Fig. S1**) was confirmed by injection of 5 µL on an Acquity UPLC system coupled to a
145 XEVO TQ-MS detector (Waters). Separation was performed at 60 °C using an Acquity UPLC BEHC18
146 column (150 × 2.1 mm I.D., 1.7 µm) at a flow rate of 0.5 mL/min with a gradient mode over 8 min. The
147 mobile phase consisted of a mixture of water with 0.1% v/v formic acid (A) and acetonitrile with 0.1% v/v
148 formic acid (B). A linear gradient from 20 to 35% B was applied for 6 min, followed by an equilibration
149 step down to 20% B over 2 min. Mass spectrometric detection was performed with electrospray ionization
150 in positive ion mode (ESI +) using MS scan mode (m/z range 400-1500). Cone and capillary voltages were
151 set at 31 V and 3.2 kV, respectively; the source temperature was kept at 150°C with a desolvation
152 temperature at 500°C and a gas flow of 800 L/h. The LC/MS TIC chromatograms were displayed using
153 MassLynx 4.1 (RRID:SCR_014271) to extract the spectrum with charge state distribution for each peak.
154 Deconvolution was performed using ESIProt 1.1.

155 Tumor inhibition

156 Animal care and experiment were approved by the local Experimental Animal Ethics Committee of the
157 BUC-CMMI (ref. CMMI-2019-01) and were conducted in compliance with the Belgian Royal Decree of 29
158 May 2013 on the protection of laboratory animals. The anti-tumoral activity of Nanofitin-MMAE drug
159 conjugates was assessed in an A431-Luc+ xenograft model. EGFR-positive A431 cells
160 (RRID:CVCL_0037) were transduced to express a luciferase gene to monitor the tumor growth and
161 indirectly assess cell viability, as described for the development of anti-EGFR chimeric antigen receptor
162 (CAR) expressing T cells (36).

163 Cells inoculation, treatment and tumor volume monitoring

164 35 six-weeks old BALB/c nude female mice (CAnN.Cg-Foxn1tm/CrJ, #194, Charles River,
165 RRID:IMSR_CRL:194) were inoculated with 5×10^6 A431 luciferase-positive (A431-Luc+)-EGFR
166 expressing cells in serum-free medium. Tumor volumes were measured 3 times a week with a caliper during
167 the whole experiment. They were calculated as follows: $V_{\text{tum}} = 0.5 \times L \times l^2$ with L = highest distance that is
168 crossing the tumor and l = lowest distance that is crossing the tumor. When tumor volume reached 90 mm^3
169 size, intravenous injections of the Nanofitin-vc-MMAE conjugates (3 mg/kg mouse, 5 mice/group) were
170 performed 3 times a week to reach a total of 12 injections per mouse, with at least one resting day between
171 two injections. 5 mice were also injected intravenously with 0.9% saline solution as controls (vehicle)
172 following the same dosing schedule. Mice were sacrificed when tumor volumes reached 2000 mm^3 . Clinical
173 signs and cohorts' survival were monitored till ten weeks after the first round of injection of Nanofitin-drug
174 conjugates.

175 Tumor cell viability monitoring by bioluminescence imaging

176 Bioluminescence imaging (BLI) of the whole mice was performed twice a week to follow *in vivo* tumor
177 growth and was expressed as the tumor growth percentage relative to day 3. Bioluminescence imaging was
178 performed by means of a Photon Imager Optima (Biospace Lab) that dynamically counted the emitted
179 photons for at least 25 min, under anesthesia (4% and 2% isoflurane for initiation and maintenance,
180 respectively) and after subcutaneous administration of 150 mg/kg of D-luciferin (Promega). Image analysis
181 was performed with M3Vision software (Biospace Lab). Regions of interest were drawn on the mice tumors,
182 and signal intensities were quantified individually for a time lapse of 5 min corresponding to the maximum
183 signal intensity plateau. Acceptance or rejection of a non-zero slope was statistically determined on the first
184 30 days corresponding to the period of treatment. The BLI data were analyzed by linear regression in
185 GraphPad Prism 6 (GraphPad Inc, RRID:SCR_002798).

186 **Anatomo-pathology analysis of tumor**

187 Animal care and experiment were approved by the local Experimental Animal Ethics Committee of the
188 BUC-CMMI (ref. CMMI-2013-05 and CMMI-2019-01) and were conducted in compliance with the
189 Belgian Royal Decree of 29 May 2013 on the protection of laboratory animals. The intra-tumoral penetration
190 of Nanofitins was assessed in an A431 xenograft model.

191 *Cells inoculation, treatment and tissue processing*

192 Eight-weeks old BALB/c nude female mice (CAnN.Cg-Foxn1^{nu}/Crl, #194, Charles River,
193 RRID:IMSR_CRL:194) were inoculated with 5×10^6 A431 EGFR-expressing cells (RRID:CVCL_0037) in
194 serum-free medium. Tumor volumes were measured and calculated as described previously. When tumor
195 volume reached 150 mm³ size, a single dose of HA-tagged Nanofitin (66 µg) or Cetuximab (1 mg, Erbitux,
196 217801, Merck) was injected intravenously (5 mice/group) to achieve the same molar dose. Mice were
197 sacrificed 90 min post injection to harvest the flanked tumors. After tumor resection and standard formalin-
198 fixed and paraffin-embedded (FFPE) tissue processing, serial tumor slices were subjected to IHC to
199 evidence CD31 in addition to Cetuximab and/or Nanofitin.

200 *Immunohistochemistry*

201 Nanofitins were HA-tagged (35) for detection by IHC, whereas Cetuximab was detected by anti-human
202 IgG. CD31/PECAM (Platelet Endothelial Cell Adhesion Molecule-1) were used to detect endothelial cells.
203 Immunostainings were performed using Discovery XT (Ventana Medical Systems, Roche Diagnostics) and
204 DABMap detection systems according to the manufacturer's recommendations. 4 µm-thick sections were
205 deparaffinized and rehydrated. Heat-induced epitope retrieval was performed using Cell Conditioning
206 Solution pH 8.4 during 36 min at 100°C. Next, slices were incubated with primary antibodies anti-CD31
207 (Cell Signaling, #77699, diluted 1:100, 2 h, RRID:AB_2722705), anti-HA-tag (Cell Signaling, #3724,
208 diluted 1:100, 1 h, RRID:AB_1549585), or anti-human IgG (Abcam, #Ab109489, diluted 1:300, 1 h,

209 RRID:AB_10863040). Subsequently, slices were incubated with a Goat Anti-Rabbit IgG Antibody (H+L),
210 Biotinylated secondary antibody (1:200, BA-1000, Vector Laboratories, RRID:AB_2313606). Sections
211 were counterstained with hematoxylin and mounted with Entellan.

212 Whole slide imaging and digital image analysis

213 The whole slides were digitized at 20x (0.453 μm side pixel) using a Hamamatsu 2.0 HT scanner
214 (Hamamatsu, RRID:SCR_021658), which was calibrated beforehand using a specific slide provided by the
215 manufacturer. Whole slide images were normalized using a methodology previously validated (37). Image
216 processing and analysis were then performed as detailed elsewhere (38). Briefly, pairs of virtual slides
217 targeting CD31 and the active compound to analyze (the Nanofitins or Cetuximab) were subjected to image
218 registration. The CD31- and compound-positive cells were then automatically detected in the aligned virtual
219 slides. In addition, up to 7 concentric tumor regions (27 μm -width each) were automatically delineated
220 around the blood vessels identified by the CD31-positive staining (**Fig. S2**), then transferred to the slide
221 images showing the compounds. The percentages of positive cells were determined as labeling indexes for
222 each compound in each concentric tumor region, and were statistically compared by one-way ANOVA in
223 GraphPad Prism 6 (GraphPad Inc, RRID:SCR_002798).

224 Data availability statement

225 The data generated in this study are available upon request from the corresponding author.

226 **Results**

227 Nanofitins show fast and deep EGFR+ tumor targeting

228 Immunohistochemistry (IHC) experiments on A431 xenograft tumors were performed to observe the
229 Nanofitins accumulation within solid tumors with a maximal contrast (32), in comparison to the reference
230 antibody Cetuximab (6). Individual positive-cells were detected for each compound, resulting in labeling
231 indexes, obtained in up to 7 concentric tumor regions delineated around the blood vessels (**Fig. S2**).

232 As expected from a xenograft model, CD31 staining revealed endothelial cells from the host vasculature,
233 infiltrated in each human tumor. Anti-IgG and anti-HA staining from consecutive slides allowed to localize
234 Cetuximab or HA-tagged Nanofitins, respectively. From the same molar dose administered systemically,
235 we report an extensive tumor penetration 90 min post-injection with HA-tagged Nanofitin D8 ($98.9\% \pm 0.7$
236 cells labeled, $n=5$, **Fig. 1**). Deep infiltration was also observed with HA-tagged Nanofitin B10 ($67.9\% \pm 14.1$,
237 $n=5$) as opposed to Cetuximab that appeared highly constrained ($24.3\% \pm 4.1$, $n=4$). A larger standard
238 deviation was observed with B10 and was attributed to blood-tinged necrosis at the core of the tumors,
239 which is commonly undergone by A431-based models. On the contrary, D8 variability is especially low due
240 to near-complete tumor labeling, resulting in more than 92% of labeled cells beyond 136 μm from the
241 vessels. In the same conditions, the Cetuximab labeling index is close to the B10 labeling index within the
242 vessel regions of interest (0 μm) and stays significantly restrained to the vessel's proximity.

243 **Regioselective assembly of Nanofitin-drug conjugates**

244 Nanofitin-drug conjugates were generated by regioselective conjugation via maleimide chemistry on a C-
245 terminal engineered-cysteine (**Fig. 2A**). Analysis by UPLC-RP/MS confirmed the conjugation of a single
246 vc-MMAE payload per Nanofitin, with purity yields ranging from 97 to 100% on the 3 different Nanofitin-
247 drug conjugates (**Fig 2B**), and undetected residual MMAE levels (under 0.4 ng/mL).

248 Binding characteristics of either the unconjugated Nanofitins or the Nanofitin-drug conjugates were
249 evaluated on human EGFR by interferometry (**Fig. 2C** and **Table 1**). The Nanofitin D8 showed slower
250 association and dissociation rates with single-digit nanomolar affinities before and after conjugation.
251 Molecules derived from the Nanofitin B10 displayed faster on- and off-rates, as described previously with
252 the parental unconjugated Nanofitin B10 (32). We noted an impact on B10 affinity upon conjugation with
253 a K_D shifting from 27.6 nM to 114.2 nM. Additionally, the anti-EGFR Nanofitins D8 and B10 were
254 demonstrated to bind human and mouse forms of EGFR (**Table 1** and **Fig. S3**). The binding of D8 constructs
255 to the human EGFR was marked with a 1-log slower off-rate, resulting in a 1-log difference of the overall

256 equilibrium constants (K_D). While the kinetic profiles appeared similar between the two forms of EGFR,
257 the binding of B10 to the human EGFR was marked with a slightly faster off-rate.

258 **Efficacy of D8-vc-MMAE in mice bearing A431-Luc+ xenografts**

259 Each Nanofitin-drug conjugate was administered intravenously 3 times a week, to reach a total of 12
260 injections, to mice bearing A431-Luc+ subcutaneous xenograft. To reduce the effect of the intrinsically
261 heterogeneous growth of A431-Luc+ tumors, the first doses were injected once tumors reached a minimum
262 of 90 mm³, resulting in a mean initial volume of 155±77mm³. Mice treated with D8-vc-MMAE showed
263 constant tumor volumes for 2 months, during both administration and follow-up periods (**Fig. 3A**). Groups
264 treated with vehicle, irrNF-vc-MMAE or B10-vc-MMAE showed significant tumor growth and multiple
265 mice reached humane endpoints before the last injection. Tumor growth was still heterogeneous within
266 groups treated with vehicle, irrNF-vc-MMAE or B10-vc-MMAE. Such variability was considered as a mark
267 of little inhibitory effect, whereas the group treated with D8-vc-MMAE presented low standard deviation
268 attributed to an efficient tumor inhibition during the treatment and the subsequent monitoring period.

269 Bioluminescence imaging (BLI) was performed for each animal to confirm the treatment efficacy. At the
270 beginning of the study, normalized bioluminescence signals defined an initial baseline between 10¹⁰ and
271 10¹¹ ph/s/cm²/sr. Treatment with recurrent injections of D8-vc-MMAE triggered a significant drop in
272 bioluminescence before the end of week 2, whereas vehicle, irrNF-vc-MMAE and B10-vc-MMAE showed
273 little effect for the first 3 weeks. The statistical analysis of the luciferase activity during the treatment period
274 demonstrated that only xenograft tumors exposed to D8-vc-MMAE validated a non-zero slope hypothesis
275 (P-value < 0.0001; **Fig. 3B**), indicating an elimination of EGFR-positive tumor cells *in vivo*. Out of the 4
276 mice monitored after 50 days, 3 showed BLI signals equivalent to the background noise (10³ ph/s/cm²/sr)
277 while the fourth mouse showed limited BLI signals (10⁶ ph/s/cm²/sr). Overall, survivors bearing tumors
278 showed a 1-to-2 log drop of signal intensities during the second month, suggesting that the anti-tumor effect
279 triggered by D8-vc-MMAE persists after clearance of the product. Each other molecule showed little anti-

280 tumor effect with tumor growth inhibitions slower than with D8-vc-MMAE, if significant. We attributed
281 drops in BLI signals after 1 month to metabolic fatigue or blood-tinged necrosis established at the core of
282 the A431-Luc+ tumors.

283 Given the necrosis-prone nature of A431-derived tumor implants (also observed by IHC, **Fig. 2**),
284 morphological analysis of the tumors was conducted and confirmed the difference between D8-vc-MMAE
285 treated mice and other animals. Efficient tumor growth inhibition was supported by reshaped, opacified and
286 hardened yellowish tumors over time with D8-vc-MMAE. In contrast, active tumors in other groups tended
287 to be softer, showed necrotic cavities at their core and were more active on their periphery.

288 The safety of the approach was evaluated by monitoring the body weight of each animal during the first 25
289 days of treatment (**Fig. 4**). Only one mouse, in the B10-vc-MMAE group, was sacrificed due to body loss
290 combined with advanced necrosis (circle). Each other animal showed constant or increasing body weight
291 over time. Three animals in the irrNF-vc-MMAE and vehicle groups reached humane endpoints and were
292 sacrificed because of the advanced necrosis of their tumor, representative of little inhibitory effect of the
293 treatment. Finally, one animal in the irrNF-vc-MMAE group and the only sacrificed animal in the D8-vc-
294 MMAE group during the treatment period tore out their xenograft and were subsequently sacrificed.

295 **Discussion**

296 The ultimate goal of anti-tumor therapies is to selectively target and kill all the tumor cells while sparing
297 healthy tissues. Conceptually, ADCs meet these requirements with the selectivity of an antibody and the
298 cytotoxic potency of its payload. Despite a growing interest in the technology and a still increasing number
299 of ADC in clinical trials (10), the attrition rate remains high and mainly driven by a lack of efficacy and
300 safety concerns. Some of the limitations of ADCs are inherently associated with the pharmacokinetic and
301 physicochemical properties of full-length antibodies such as hepatic clearance, a slow tumor uptake, avidity
302 via their two binding sites and a long plasma half-life.

303 In this study, we evaluated the fitness of the small Nanofitin scaffold for the generation of drug conjugates,
304 using the clinically validated protease-labile valine-citrulline linker and the auristatin derivative MMAE as
305 a cytotoxic payload (**Fig. 2A**). Tumor targeting was achieved using anti-EGFR Nanofitins (32) D8 and B10,
306 which compete with Cetuximab (**Fig. S4**), cross-react with both human and murine EGFR, and have similar
307 affinity constants (K_D of 5.56 and 27.6 nM respectively, **Table 1**). These affinities fall in the range described
308 for selective EGFR-positive tumors targeting over healthy EGFR-expressing tissues (39). We observed that
309 while targeting an overlapping epitope (**Fig. S4**), the two Nanofitin ligands differ from Cetuximab (40) in
310 their ability to cross-react with mouse EGFR. Such cross-reactivity, beneficial for therapeutic development
311 to demonstrate the absence of adverse effects, may be attributed to their in vitro selection process (27–34)
312 that is not restricted by immunization determinism. The anti-EGFR Nanofitin D8, initially referred as
313 α EGFR_NF2, was internalized after incubation with A431 carcinoma cells (32). In similar conditions, no
314 meaningful internalization of B10 could be observed, indicating that these two Nanofitins exhibit a different
315 ability at inducing receptor-mediated endocytosis.

316 The two HA-tagged Nanofitins, able to engage the cell surface receptor (**Fig. S5**), displayed a broad
317 intratumoral infiltration 90 min after their tail-vein injection in an A431 tumor xenograft murine model, as
318 shown by IHC (**Fig. 1**). IHC results revealed an engagement of $67.9\% \pm 14.1$ and $98.9\% \pm 0.7$ of the tumor
319 cells, respectively for B10 and D8. The penetration of D8 was highly homogeneous within all of the tumor,
320 while the level of cells labelled by B10 appeared to decrease down from 75% starting from up to 80 μ m
321 away from the closest vessel to 25% in the deepest regions (136+ μ m). Further evaluations would be
322 required to decipher whether their differential accumulation level is linked to their different dissociation
323 rates ($0.90 \times 10^{-2} \text{ s}^{-1}$ for D8-HA and $10.18 \times 10^{-2} \text{ s}^{-1}$ for B10-HA) or other physicochemical properties (e.g.:
324 internalization, charge). This IHC dataset highlights the faster penetration potential of the anti-EGFR
325 Nanofitins as compared to the antibody Cetuximab at this time point. In our study, only $24.3\% \pm 4.1$ of the
326 tumor cells were labelled by Cetuximab, which was found mainly restricted within the perivascular space
327 in an area of up to 27 μ m from the vasculature. Our results are in agreement with the finding of Lee and

328 Tannock, who also reported a staining of Cetuximab mainly in the perivascular space of A431 xenografts
329 with the same injected dose (1 mg) (6). The binding site barrier has been reported to slow down the diffusion
330 rate of Cetuximab (6) in the high EGFR-expressing tumors A431 ($2\text{-}3\times 10^6$ EGFR molecules per cell), with
331 higher avidity in a context of high target density. The monovalent binding kinetic profiles of the anti-EGFR
332 Nanofitins could also contribute to their faster diffusion in this tumor xenograft model as compared to that
333 of the bivalent antibody Cetuximab. In another study comparing several drug conjugate formats, Nessler *et*
334 *al.* also reported that a monovalent format could result in a better anti-tumor efficacy due to a higher
335 penetration and an increased number of cells exposed to lethal payload doses (41). It remains to be
336 investigated whether the binding kinetics of the anti-EGFR Nanofitins also support high accumulation in
337 other tumors expressing a lower level of the tumor antigen. Alternatively, both affinity (30) and valence of
338 Nanofitins can be tuned using straightforward protein engineering strategies.

339 Nanofitin-vc-MMAE drug conjugates were generated by engineering the Nanofitins to exhibit a single and
340 solvent accessible cysteine. It enables thiol-based regioselective conjugation with the maleimide activated
341 MMAE toxin, leading to highly homogeneous conjugates with overall purity of $\geq 97\%$ (**Fig. 2B**). Despite
342 the high tumor accumulation observed for both D8 and B10 Nanofitins, only D8-vc-MMAE compound
343 yielded high anti-tumor activity compared to the controls treated with the vehicle only or with a non-
344 targeting drug conjugate based on a Nanofitin that binds specifically to hen-egg white lysozyme (irrNF,
345 irrelevant Nanofitin (42, 43)). The activity of D8-vc-MMAE was confirmed by both a strong inhibition of
346 the tumor growth as well as reduction of the luciferase activity, hence the cell viability, within the residual
347 tumor tissue (**Fig. 3**). The differential anti-tumoral effect between D8- and B10-vc-MMAE drug conjugates
348 suggests that efficient tumor targeting, inferred from IHC with HA-tagged Nanofitins derived from D8 and
349 B10, is not sufficient for a therapeutic activity. Bennett *et al.* compared the anti-tumor efficacy of MMAE
350 and MMAF cytotoxic payload targeted with a bicycle peptide (44). Greater tumor growth inhibition was
351 observed with the MMAE-based drug conjugate. The difference of activity was attributed to the bystander
352 activity of MMAE that is absent with MMAF. However, whether internalization was required for the

353 activation of the toxin, or could result from its extracellular cleavage in the tumor microenvironment,
354 remained elusive and the authors concluded that it is likely that it results from a combination of both. While
355 we cannot rule out the possibility that the toxin was activated extracellularly in our study, the lack of anti-
356 tumor activity observed with the non-internalizing B10-MMAE drug conjugate suggests that the
357 internalization may be required for therapeutically relevant toxin release in the preclinical model that we
358 used. Interestingly, monitoring of mice over 2 months showed that D8-vc-MMAE prevented recurrence of
359 the tumor, as demonstrated by morphological analysis and bioluminescence imaging, suggesting that the
360 efficient tumor penetration of the drug could give rise to complete remission. Aside from its high anti-tumor
361 activity, i.e., its high local cytotoxicity, we observed no sign of systemic toxicity upon D8-vc-MMAE
362 administration, as evidenced by the constant body weights during treatment (**Fig. 4**). We anticipate that such
363 a behavior *in vivo* is encouraging for future toxicity studies, as the Nanofitin D8 is able to bind to EGFR not
364 only from the xenograft but also from the host, whilst we acknowledge a 1-log affinity difference for the
365 two receptors (**Table 1**). To maximize exposure, dosing schedule of the Nanofitin-drug conjugates consisted
366 in 3 intravenous injections a week, up to a total of 12 injections. It would be interesting to evaluate the
367 duration of tumor exposure to cytotoxic dose of the payload upon a bolus administration of the Nanofitin-
368 drug conjugate to rationalize the administration scheme. A sustained tumor exposure to the toxin, supporting
369 a weekly dosing, was reported with a single bolus injection of bicycle peptide-MMAE conjugate (44).
370 Reducing the administration frequency of the Nanofitin-vc-MMAE drug conjugate shall foster the
371 translatability of this approach into clinical setting.

372 In conclusion, we demonstrated with this study that the Nanofitin technology exhibits the attributes for an
373 efficient and safe tumor targeting of potent cytotoxic payloads like the auristatin derivative MMAE. Owing
374 to its small molecular size and monovalent format, the anti-EGFR Nanofitin-drug conjugate D8-vc-MMAE
375 penetrated deeply within A431 tumor tissue, yielding to a targeting of nearly all of the tumor cells. Its ability
376 at triggering receptor-mediated endocytosis may play a critical role in facilitating the efficient release of the

377 MMAE toxin and subsequent anti-tumor effect. Additionally, the rapid clearance of Nanofitins by renal
378 filtration provides the potential to overcome one of the current safety concerns with ADCs.

379 **Acknowledgments**

380 This project was partially sponsored from November 2017 to February 2020 by a grant from Eurostars / the
381 European Commission via Banque Publique d'Investissement for France (DOS0059903), the Agência
382 Nacional de Inovação for Portugal (E!11391 ONCOFITIN) and Innosuisse for Switzerland (1315001273).
383 CMMI is supported by the European Regional Development Fund and the Walloon Region. GVS and GD
384 are also supported by the Fondation ULB, the Fonds Erasme and “Association Vinçotte Nuclear” (AVN).

385 We are grateful to Justine Picot, Anaëlle Perrocheau, Harmony Gorré, Chloé Savignard, Anne Chevrel, Léo
386 Candela, Caroline Roze, Rémi Gaillard, Elise Enouf and Maurine Fleury from Affilogic for their
387 involvement and technical support. We acknowledge Sónia Mendes, Rute P. Eleutério, Mónica Thomaz and
388 Filipe Pinto for their technical support on the project at iBET. We thank the Center for Microscopy and
389 Molecular Imaging (CMMI) for their contribution to the experiments with the xenograft model, especially
390 Cedric Balsat, Justine Allard, Yves-Rémy Van Eycke, Coraline De Maeseneire, Nicolas Passon, Isabelle
391 Salmon and Christine Decaestecker.

392 **References**

- 393 1. S. J. C. Mancini, K. Balabanian, I. Corre, J. Gavard, G. Lazennec, M.-C. Le Bousse-Kerdilès, F.
394 Louache, V. Maguer-Satta, N. M. Mazure, F. Mehta-Grigoriou, J.-F. Peyron, V. Trichet, O.
395 Herault, Deciphering Tumor Niches: Lessons From Solid and Hematological Malignancies. *Front.*
396 *Immunol.* **12** (2021). doi:10.3389/fimmu.2021.766275
- 397 2. M. R. Dreher, W. Liu, C. R. Michelich, M. W. Dewhirst, F. Yuan, A. Chilkoti, Tumor Vascular
398 Permeability, Accumulation, and Penetration of Macromolecular Drug Carriers. *JNCI J. Natl.*
399 *Cancer Inst.* **98**, 335–344 (2006). doi:10.1093/jnci/djj070

- 400 3. K. Tsuchikama, Z. An, Antibody-drug conjugates: recent advances in conjugation and linker
401 chemistries. *Protein Cell*. **9**, 33–46 (2018). doi:10.1007/s13238-016-0323-0
- 402 4. S. Ponziani, G. Di Vittorio, G. Pitari, A. M. Cimini, M. Ardini, R. Gentile, S. Iacobelli, G. Sala, E.
403 Capone, D. J. Flavell, R. Ippoliti, F. Giansanti, Antibody-drug conjugates: The new frontier of
404 chemotherapy. *Int. J. Mol. Sci.* **21**, 1–28 (2020). doi:10.3390/ijms21155510
- 405 5. J. Zhao, Cancer stem cells and chemoresistance: The smartest survives the raid. *Pharmacol. Ther.*
406 **160**, 145–158 (2016). doi:10.1016/j.pharmthera.2016.02.008
- 407 6. C. M. Lee, I. F. Tannock, The distribution of the therapeutic monoclonal antibodies cetuximab and
408 trastuzumab within solid tumors. *BMC Cancer*. **10** (2010). doi:10.1186/1471-2407-10-255
- 409 7. K. T. Xenaki, S. Oliveira, P. M. P. van Bergen en Henegouwen, Antibody or antibody fragments:
410 Implications for molecular imaging and targeted therapy of solid tumors. *Front. Immunol.* **8**
411 (2017). doi:10.3389/fimmu.2017.01287
- 412 8. M. Juweid, R. Neumann, C. Paik, M. J. Perez-Bacete, J. Sato, W. van Osdol, J. N. Weinstein,
413 Micropharmacology of monoclonal antibodies in solid tumors: direct experimental evidence for a
414 binding site barrier. *Cancer Res.* **52**, 5144–53 (1992). Available at
415 <http://www.ncbi.nlm.nih.gov/pubmed/1327501>
- 416 9. A. Labani-Motlagh, M. Ashja-Mahdavi, A. Loskog, The Tumor Microenvironment: A Milieu
417 Hindering and Obstructing Antitumor Immune Responses. *Front. Immunol.* **11**, 1–22 (2020).
418 doi:10.3389/fimmu.2020.00940
- 419 10. A. Q. Dean, S. Luo, J. D. Twomey, B. Zhang, Targeting cancer with antibody-drug conjugates:
420 Promises and challenges. *MAbs*. **13** (2021). doi:10.1080/19420862.2021.1951427
- 421 11. C. Vasalou, G. Helmlinger, B. Gomes, A Mechanistic Tumor Penetration Model to Guide
422 Antibody Drug Conjugate Design. *PLoS One*. **10**, 1–20 (2015). doi:10.1371/journal.pone.0118977

- 423 12. N. Joubert, A. Beck, C. Dumontet, C. Denevault-Sabourin, Antibody–drug conjugates: The last
424 decade. *Pharmaceuticals*. **13** (2020), pp. 1–30. doi:10.3390/ph13090245
- 425 13. C. Esnault, D. Schrama, R. Houben, S. Guyétant, A. Desgranges, C. Martin, P. Berthon, M. C.
426 Viaud-Massuard, A. Touzé, T. Kervarrec, M. Samimi, Antibody–Drug Conjugates as an Emerging
427 Therapy in Oncodermatology. *Cancers (Basel)*. **14** (2022). doi:10.3390/cancers14030778
- 428 14. M. J. Eigenmann, L. Fronton, H. P. Grimm, M. B. Otteneder, B. F. Krippendorff, Quantification of
429 IgG monoclonal antibody clearance in tissues. *MAbs*. **9**, 1007–1015 (2017).
430 doi:10.1080/19420862.2017.1337619
- 431 15. C. M. Mckertish, V. Kayser, Advances and limitations of antibody drug conjugates for cancer.
432 *Biomedicines*. **9** (2021). doi:10.3390/biomedicines9080872
- 433 16. R. M. Hoffmann, B. G. T. Coumbe, D. H. Josephs, S. Mele, K. M. Ilieva, A. Cheung, A. N. Tutt, J.
434 F. Spicer, D. E. Thurston, S. Crescioli, S. N. Karagiannis, Antibody structure and engineering
435 considerations for the design and function of Antibody Drug Conjugates (ADCs).
436 *Oncoimmunology*. **7** (2018). doi:10.1080/2162402X.2017.1395127
- 437 17. K. D. Orcutt, G. P. Adams, A. M. Wu, M. D. Silva, C. Harwell, J. Hoppin, M. Matsumura, M.
438 Kotsuma, J. Greenberg, A. M. Scott, R. A. Beckman, Molecular Simulation of Receptor
439 Occupancy and Tumor Penetration of an Antibody and Smaller Scaffolds: Application to
440 Molecular Imaging. *Mol. Imaging Biol.* **19**, 656–664 (2017). doi:10.1007/s11307-016-1041-y
- 441 18. M. M. Schmidt, K. D. Wittrup, A modeling analysis of the effects of molecular size and binding
442 affinity on tumor targeting. *Mol. Cancer Ther.* **8**, 2861–2871 (2009). doi:10.1158/1535-
443 7163.MCT-09-0195
- 444 19. M. Srinivasarao, C. V. Galliford, P. S. Low, Principles in the design of ligand-targeted cancer
445 therapeutics and imaging agents. *Nat. Rev. Drug Discov.* **14** (2015), pp. 203–219.

- 446 doi:10.1038/nrd4519
- 447 20. S. Cazzamalli, A. Dal Corso, F. Widmayer, D. Neri, Chemically defined antibody- and small
448 molecule-drug conjugates for in vivo tumor targeting applications: A comparative analysis. *J. Am.*
449 *Chem. Soc.* **140**, 1617–1621 (2018). doi:10.1021/jacs.7b13361
- 450 21. Z. Li, B. F. Krippendorff, S. Sharma, A. C. Walz, T. Lavé, D. K. Shah, Influence of molecular size
451 on tissue distribution of antibody fragments. *MAbs.* **8**, 113–119 (2016).
452 doi:10.1080/19420862.2015.1111497
- 453 22. Z. Li, Y. Li, H. P. Chang, H. Y. Chang, L. Guo, D. K. Shah, Effect of size on solid tumor
454 disposition of protein therapeutics. *Drug Metab. Dispos.* **47**, 1136–1145 (2019).
455 doi:10.1124/dmd.119.087809
- 456 23. G. Bennett, A. Brown, G. Mudd, P. Huxley, K. van Rietschoten, S. Pavan, L. Chen, S. Watcham, J.
457 Lahdenranta, N. Keen, MMAE delivery using the bicycle toxin conjugate BT5528. *Mol. Cancer*
458 *Ther.* **19**, 1385–1394 (2020). doi:10.1158/1535-7163.MCT-19-1092
- 459 24. ClinicalTrials.gov, Identifier NCT03486730, BT1718 in Patients With Advanced Solid Tumours
460 (2018 Apr 3 -). *Natl. Libr. Med.* (2000). Available at
461 <https://clinicaltrials.gov/ct2/show/NCT03486730>
- 462 25. ClinicalTrials.gov, Identifier NCT04180371, Study BT5528-100 in Patients With Advanced Solid
463 Tumors Associated With EphA2 Expression (2019 Nov 27 -). *Natl. Libr. Med.* (2000). Available
464 at <https://clinicaltrials.gov/ct2/show/NCT04180371>
- 465 26. K. Škrlec, B. Štrukelj, A. Berlec, Non-immunoglobulin scaffolds: a focus on their targets. *Trends*
466 *Biotechnol.* **33** (2015). doi:10.1016/j.tibtech.2015.03.012
- 467 27. G. Béhar, M. Bellinzoni, M. Maillason, L. Paillard-Laurance, P. M. Alzari, X. He, B. Mouratou,
468 F. Pecorari, Tolerance of the archaeal Sac7d scaffold protein to alternative library designs:

- 469 characterization of anti-immunoglobulin G Affitins. *Protein Eng. Des. Sel.* **26**, 267–75 (2013).
470 doi:10.1093/protein/gzs106
- 471 28. S. Huet, H. Gorre, A. Perrocheau, J. Picot, M. Cinier, “Use of the Nanofitin alternative scaffold as
472 a GFP-ready fusion tag” (2015).
- 473 29. A. Chevrel, L. Candela, E. Innocenti, C. Golibrzuch, R. Skudas, A. Schwämmle, M. J. T.
474 Carrondo, O. Kitten, M. Nissum, R. J. S. Silva, Development of versatile affinity-based system for
475 one step purification process: Case of Group A Streptococcus vaccine. *Biotechnol. Bioeng.* (2022).
476 doi:10.1002/bit.28199
- 477 30. J. Garlich, M. Cinier, A. Chevrel, A. Perrocheau, D. J. Eyerma, M. Orme, O. Kitten, L. Scheibler,
478 Discovery of APL-1030, a Novel, High-Affinity Nanofitin Inhibitor of C3-Mediated Complement
479 Activation. *Biomolecules.* **12** (2022). doi:10.3390/biom12030432
- 480 31. N. Michot, A. Guyochin, M. Cinier, C. Savignard, O. Kitten, M.-H. Pascual, S. Pouzieux, M.-L.
481 Ozoux, P. Verdier, P. Vicat, J. Dumas, Albumin binding Nanofitins, a new scaffold to extend half-
482 life of biologics – a case study with exenatide peptide. *Peptides.* **152**, 170760 (2022).
483 doi:10.1016/j.peptides.2022.170760
- 484 32. M. Goux, G. Becker, H. Gorré, S. Dammico, A. Desselle, D. Egrise, N. Leroi, F. Lallemand, M.
485 A. Bahri, G. Doumont, A. Plenevaux, M. Cinier, A. Luxen, Nanofitin as a New Molecular-Imaging
486 Agent for the Diagnosis of Epidermal Growth Factor Receptor Over-Expressing Tumors.
487 *Bioconjug. Chem.* **28**, 2361–2371 (2017). doi:10.1021/acs.bioconjchem.7b00374
- 488 33. V. Kalichuk, A. Renodon-Corniere, G. Behar, F. Carrion, G. Obal, M. Maillason, B. Mouratou, V.
489 Preat, F. Pecorari, A novel, smaller scaffold for Affitins: Showcase with binders specific for
490 EpCAM. *Biotechnol. Bioeng.* (2017). doi:10.1002/bit.26463
- 491 34. G. Marcion, F. Hermetet, F. Neiers, B. Uyanik, L. Dondaine, A. M. M. Dias, L. Da Costa, M.

- 492 Moreau, P. S. Bellaye, B. Collin, J. Gobbo, L. Briand, R. Seigneuric, O. Kitten, M. Cinier, C.
493 Garrido, Nanofitins targeting heat shock protein 110: An innovative immunotherapeutic modality
494 in cancer. *Int. J. Cancer*. **148**, 3019–3031 (2021). doi:10.1002/ijc.33485
- 495 35. J. Field, J. Nikawa, D. Broek, B. MACDONALD, It Linda Rodgers, I. A. Wilson, R. A. Lerner, M.
496 WIGLERI, “Purification of a RAS-Responsive Adenylyl Cyclase Complex from *Saccharomyces*
497 *cerevisiae* by Use of an Epitope Addition Method Downloaded from” (1988). Available at
498 <http://mcb.asm.org/>
- 499 36. S. Albert, C. Arndt, A. Feldmann, R. Bergmann, D. Bachmann, S. Koristka, F. Ludwig, P. Ziller-
500 Walter, A. Kegler, S. Gärtner, M. Schmitz, A. Ehninger, M. Cartellieri, G. Ehninger, H. J.
501 Pietzsch, J. Pietzsch, J. Steinbach, M. Bachmann, A novel nanobody-based target module for
502 retargeting of T lymphocytes to EGFR-expressing cancer cells via the modular UniCAR platform.
503 *Oncoimmunology*. **6** (2017). doi:10.1080/2162402X.2017.1287246
- 504 37. Y. R. Van Eycke, J. Allard, I. Salmon, O. Debeir, C. Decaestecker, Image processing in digital
505 pathology: An opportunity to solve inter-batch variability of immunohistochemical staining. *Sci.*
506 *Rep.* **7**, 1–15 (2017). doi:10.1038/srep42964
- 507 38. L. Godin, C. Balsat, Y. R. Van Eycke, J. Allard, C. Royer, M. Rummelink, I. Pastushenko, N.
508 D’Haene, C. Blanpain, I. Salmon, S. Rorive, C. Decaestecker, A novel approach for quantifying
509 cancer cells showing hybrid epithelial/mesenchymal states in large series of tissue samples:
510 Towards a new prognostic marker. *Cancers (Basel)*. **12** (2020). doi:10.3390/cancers12040906
- 511 39. T. Crombet, M. Osorio, T. Cruz, C. Roca, R. Del Castillo, R. Mon, N. Iznaga-Escobar, R.
512 Figueredo, J. Koropatnick, E. Renginfo, E. Fernández, D. Álvarez, O. Torres, M. Ramos, I.
513 Leonard, R. Pérez, A. Lage, Use of the humanized anti-epidermal growth factor receptor
514 monoclonal antibody h-R3 in combination with radiotherapy in the treatment of locally advanced
515 head and neck cancer patients. *J. Clin. Oncol.* **22**, 1646–1654 (2004).

516 doi:10.1200/JCO.2004.03.089

- 517 40. B. A. W. Hoeben, J. D. M. Molkenboer-Kuenen, W. J. G. Oyen, W. J. M. Peeters, J. H. A. M.
518 Kaanders, J. Bussink, O. C. Boerman, Radiolabeled cetuximab: Dose optimization for epidermal
519 growth factor receptor imaging in a head-and-neck squamous cell carcinoma model. *Int. J. Cancer.*
520 **129**, 870–878 (2011). doi:10.1002/ijc.25727
- 521 41. I. Nessler, E. Khera, S. Vance, A. Kopp, Q. Qiu, T. A. Keating, A. O. Abu-Yousif, T. Sandal, J.
522 Legg, L. Thompson, N. Goodwin, G. M. Thurber, Increased Tumor Penetration of Single-Domain
523 Antibody–Drug Conjugates Improves In Vivo Efficacy in Prostate Cancer Models. *Cancer Res.* **80**,
524 1268–1278 (2020). doi:10.1158/0008-5472.CAN-19-2295
- 525 42. M. Cinier, M. Petit, M. N. Williams, R. M. Fabre, F. Pecorari, D. R. Talham, B. Bujoli, C. Tellier,
526 Bisphosphonate adaptors for specific protein binding on zirconium phosphonate-based
527 microarrays. *Bioconjug. Chem.* **20**, 2270–7 (2009). doi:10.1021/bc9002597
- 528 43. A. Correa, S. Pacheco, A. E. Mechaly, G. Obal, G. Bé Har, B. Mouratou, P. Oppezzo, P. M. Alzari,
529 F. Dé, R. Pecorari, Potent and Specific Inhibition of Glycosidases by Small Artificial Binding
530 Proteins (Affitins). *PLoS One.* **9** (2014). doi:10.1371/journal.pone.0097438
- 531 44. M. P. Deonarain, Q. Xue, Tackling solid tumour therapy with small-format drug conjugates. *Antib.*
532 *Ther.* **3** (2020), pp. 237–245. doi:10.1093/abt/tbaa024

533 Tables

	Human EGFR				Mouse EGFR			
	K _D (nM)	k _{on} (10 ⁶ M ⁻¹ .s ⁻¹)	k _{off} (10 ⁻² s ⁻¹)	R ²	K _D (nM)	k _{on} (10 ⁶ M ⁻¹ .s ⁻¹)	k _{off} (10 ⁻² s ⁻¹)	R ²
D8	5.56±0.05	1.55±0.01	0.86±0.00	0.96	59.69±3.01	1.74±0.08	10.40±0.16	0.94
D8-HA	5.29±0.05	1.70±0.02	0.90±0.00	0.96	54.17±2.61	1.77±0.08	9.59±0.14	0.94
D8-vc-MMAE	5.85±0.08	3.88±0.05	2.27±0.01	0.99	N.D.	N.D.	N.D.	N.D.
B10*	27.6	1.90	5.24	0.99	83.0	1.41	11.7	0.98
B10-HA	48.80±1.39	2.09±0.06	10.18±0.09	0.98	143.60±5.92	2.68±0.10	38.44±0.53	0.99
B10-vc-MMAE	114.20±6.40	2.03±0.11	23.14±0.39	0.98	N.D.	N.D.	N.D.	N.D.

534
535 **Table 1. Affinity determination against human and mouse EGFR.** Binding characteristics of the anti-
536 EGFR Nanofitins and Nanofitin-drug conjugates determined by biolayer interferometry on human and
537 mouse EGFR. D8 and B10: Nanofitins without C-terminal tag. D8-HA and B10-HA: Nanofitins with a C-
538 terminal HA-tag. D8-vc-MMAE and B10-vc-MMAE: Nanofitin-drug conjugates with a C-terminal
539 payload. *According to Goux, *et al* (32). N.D.: Not determined.

540 **Figure legends**

541 **Fig. 1. Intratumoral infiltration 90 min after systemic administration.** (A) Intratumoral infiltration of
542 anti-EGFR Nanofitins or Cetuximab, revealed by anti-HA and anti-IgG immunohistochemistry,
543 respectively. Host vasculature is revealed by anti-CD31 staining of consecutive slice sections. Zoom of
544 selected regions illustrates EGFR labeling at the vessel proximity. (B) Labeling index, based on cells
545 positively labeled, in the whole tumor. (C) Labeling index relative to the distance from the closest blood
546 vessel. ****: P-value < 0.0001; ***: P-value < 0.0005.

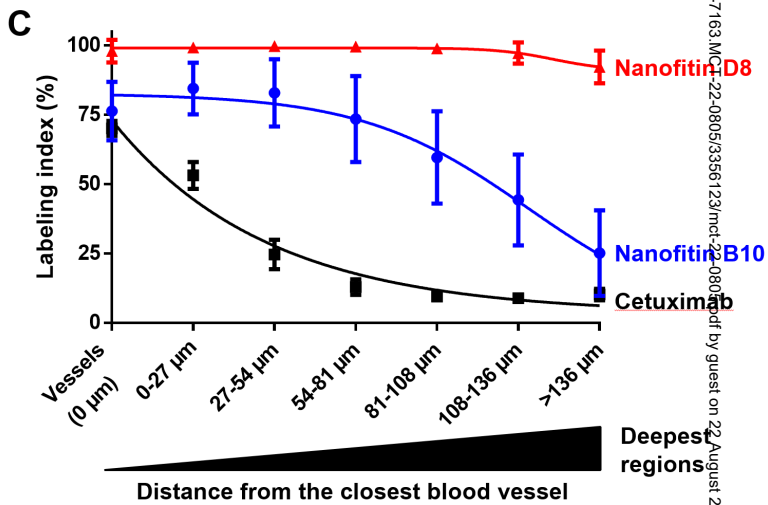
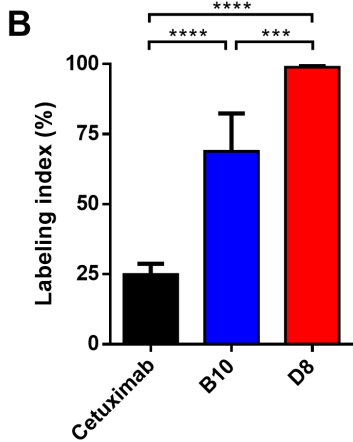
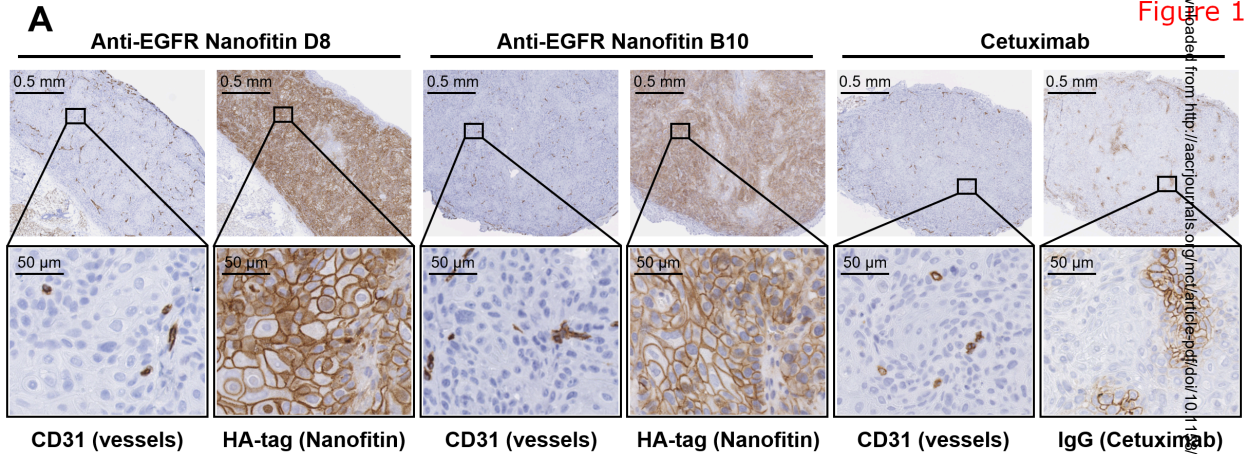
547 **Fig. 2. Biochemical profiles of Nanofitin-drug conjugates.** (A) Schematic representation of a Nanofitin-
548 drug conjugate. The single chain of the Nanofitin scaffold (rainbow cartoon) is engineered to target EGFR
549 by randomizing up to 14 amino acids (spheres in lieu of carbon alpha). Each Nanofitin is genetically fused
550 to a C-terminal cysteine (gray/yellow stick) to allow the regioselective chemistry on the only thiol group.
551 The vc-MMAE payload (structural formula) is coupled via its maleimide-based moiety (black) and releases
552 the MMAE toxin (red) after proteolytic cleavage of the valine-citrulline linker (orange). (B) UPLC-RP/MS
553 profiles. Peaks were identified by ESI-MS spectral deconvolution to determine their mass. Percentages of
554 corresponding species were determined from the area under the absorbance curves. (C) Determination of
555 the binding characteristics of the anti-EGFR Nanofitin-drug conjugates D8-vc-MMAE (left) and B10-vc-
556 MMAE (right) by biolayer interferometry on human EGFR, using the anti-EGFR Nanofitin at
557 concentrations of 500, 125, 31.25, and 7.81 nM. Fittings are represented as solid red lines.

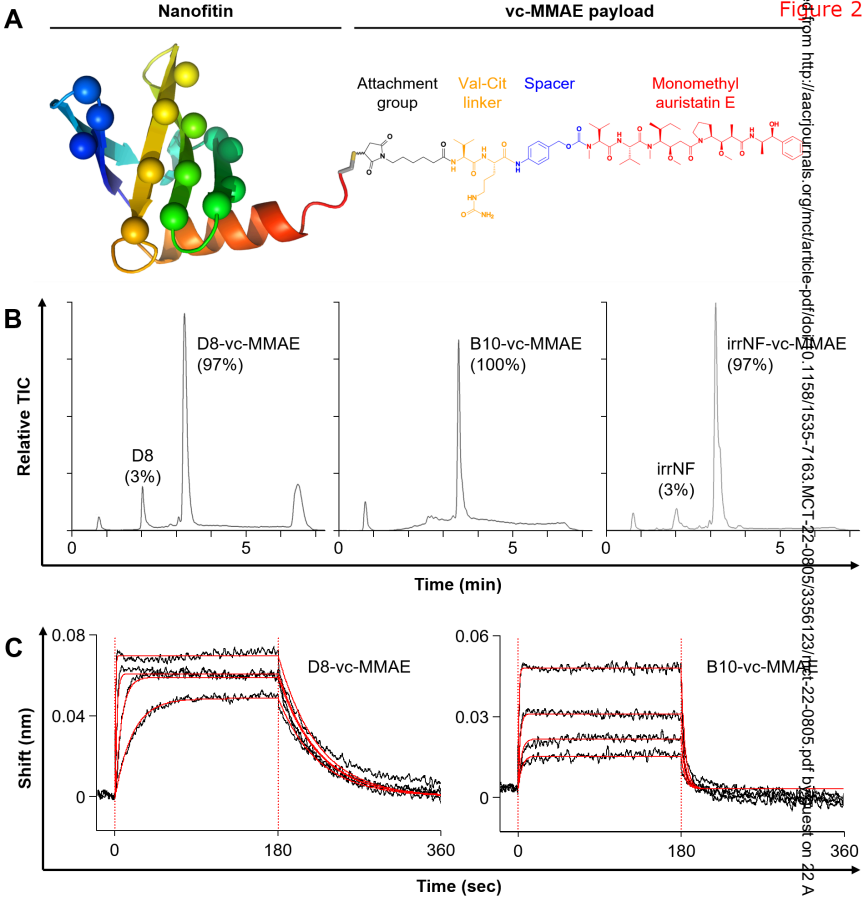
558 **Fig. 3. Therapeutic efficacy of D8-vc-MMAE against A431-Luc+ tumor xenograft model in nude mice.**

559 Mice were treated with 3 mg/kg of Nanofitin-drug conjugates or vehicle. Time zero of the treatment is set
560 when tumor volume reaches 90 mm³. Gray arrows indicate the period of treatment. (A) Individual tumor
561 growing curves. (B) Individual bioluminescence imaging curves (solid) and simple linear regression curve
562 during treatment (dashed) statistically compared to a non-zero slope hypothesis. ****: P-value < 0.0001;
563 n.s.: not significant.

564 **Fig. 4. Body weight monitoring during the first 25 days of treatment.** White symbol with black outline:

565 mouse sacrificed because of torn out tumor (diamond), advanced necrosis (triangle) or body-weight loss
566 and necrosis (circle).





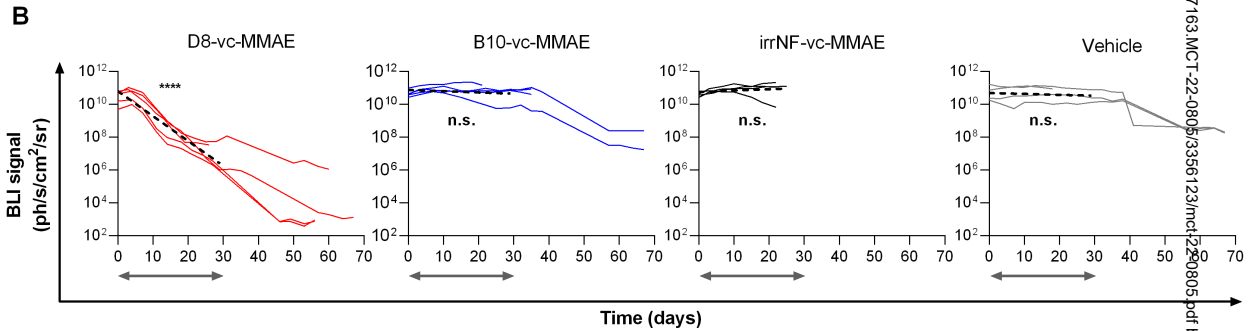
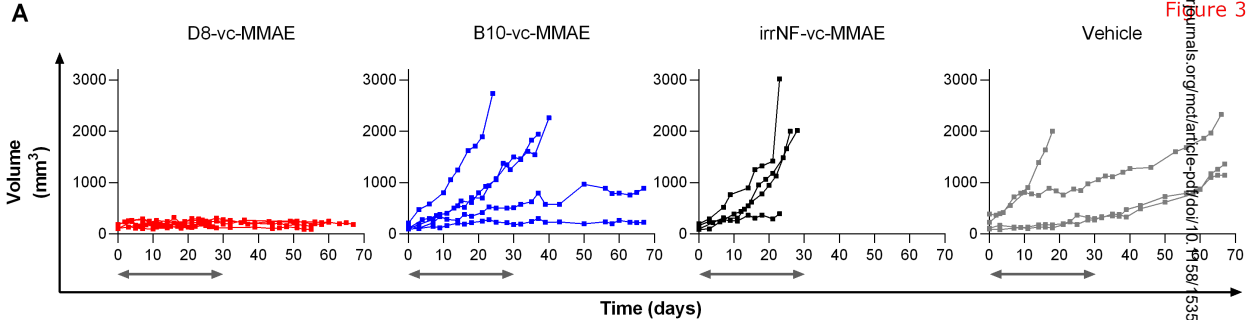


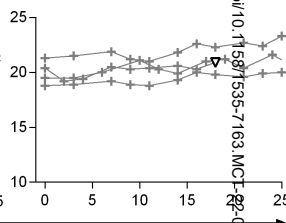
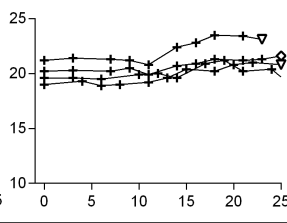
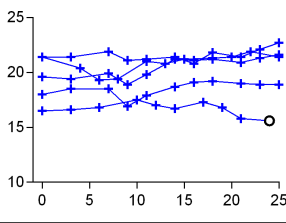
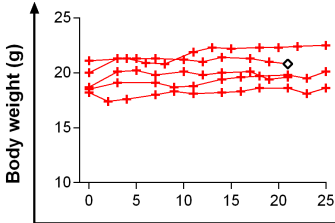
Figure 4

D8-vc-MMAE

B10-vc-MMAE

irrNF-vc-MMAE

Vehicle

**Time after initial dose (days)**